

Outflow–cloud interaction as the possible origin of the peculiar radio emission in the tidal disruption event AT2018cqh

LEI YANG,¹ XINWEN SHU,¹ GUOBIN MOU,² YONGQUAN XUE,^{3,4} LUMING SUN,¹ FABAO ZHANG,¹ ZHUMAO ZHANG,¹ YIBO WANG,³ TAO WU,¹ NING JIANG,^{3,4} HUCHENG DING,¹ AND TINGGUI WANG^{3,4}

¹*Department of Physics, Anhui Normal University, Wuhu, Anhui, 241002, China*

²*Department of Physics and Institute of Theoretical Physics, Nanjing Normal University, Nanjing 210023, China*

³*Department of Astronomy, University of Science and Technology of China, Hefei, Anhui 230026, China*

⁴*School of Astronomy and Space Science, University of Science and Technology of China, Hefei, Anhui, 230026, China*

ABSTRACT

AT2018cqh is a unique optical tidal disruption event (TDE) discovered in a dwarf galaxy exhibiting delayed X-ray and radio flares. We present the results from high-resolution VLBA and e-MERLIN radio observations of AT2018cqh extending to $\delta t \sim 2250$ days post discovery, which reveal a compact radio emission, unresolved at a scale of $\lesssim 0.13$ pc at 7.6 GHz, with a high brightness temperature of $T_b \gtrsim 4.03 \times 10^9$ K. The radio spectral energy distribution (SED) is found to gradually shift towards a higher peak flux density and frequency over a period of ~ 1000 days. An equipartition analysis suggests that there is a little change in the radio emitting region over this period, while the electron density increases by a factor of 3. The radio light curve at 0.89 GHz continues to rise, with a bump feature lasting for 240 days. These properties are in contrast to the predictions of standard shockwave model from a diffuse circumnuclear medium, but could be explained if dense clouds exist in the circumnuclear environment. The latter scenario is supported by our hydrodynamic simulations of the interaction of TDE outflow with a cloud, which can reproduce the temporal evolution in the radio SED. This work highlights the importance of the outflow–cloud interaction in explaining the delayed, fast-rising radio emission observed in some TDEs, especially those occurring in galaxies with pre-existing AGN activity.

Keywords: Accretion (14); Active galactic nuclei (16); Tidal disruption (1696); Radio transient sources (2008)

1. INTRODUCTION

When a star passes too close to a supermassive black hole (SMBH), it can be squeezed and torn apart once the tidal force of the SMBH exceeds the star’s self-gravity (Rees 1988), which is called a tidal disruption event (TDE). Approximately half of the debris remains in orbits bound to the black hole, while other parts are flung out on hyperbolic orbits (Rees 1988). The bound stellar debris will circularize and form an accretion disk, generating luminous flares typically peaking in X-rays and ultraviolet (Saxton et al. 2020; Gezari 2021). TDEs enable a direct probe to the transient accretion onto SMBHs, as well as the subsequent launch of jet and outflow. When a jet/outflow propagates outward, it will interact with the diffuse circumnuclear medium (CNM). The shock process in CNM can accelerate electrons in magnetic field, producing a bright flare of radio synchrotron emission (De Colle et al. 2012; Lu & Kumar 2018; Alexander et al. 2020; Fangyi et al. 2025). Therefore, radio observations of

TDEs are not only essential to infer the properties of jet and outflow, but also to illuminate the environment around otherwise dormant SMBHs (Alexander et al. 2020).

So far only four TDEs have been securely identified to have powerful on-axis relativistic jets (Burrows et al. 2011; Brown et al. 2015; Pasham et al. 2015; Andreoni et al. 2022), which were readily detected at radio frequencies since discovery. Most radio-emitting TDEs could be related to off-axis jets (Lei et al. 2016; Mattila et al. 2018; Sfaradi et al. 2024), sub-relativistic (Cendes et al. 2022, 2025), or non-relativistic wide-angle outflows (e.g., Alexander et al. 2016, 2017; Cendes et al. 2021, 2022; Goodwin et al. 2022, 2023a,b, 2024), with radio luminosities about two orders of magnitude lower than on-axis jetted TDEs. Recently, Cendes et al. (2024) present the results from radio follow-up observations of 23 optical TDEs and find that $\sim 40\%$ of them exhibit radio brightening hundreds to thousands of days after the discovery, indicating the ubiquitous late radio emission from TDEs though the origin remains unclear. More interestingly, a few TDEs display steeply rising light curves in the delayed radio emission (Horesh et al. 2021; Cendes et al. 2022; Zhang et al. 2024; Sfaradi et al. 2025), requiring a temporal power-law in-

dex steeper than t^4 —a behavior inconsistent with the predictions of standard model that a single outflow (either relativistic or sub-relativistic) is launched into the CNM promptly following the TDE.

Several scenarios have been proposed to explain these late-time and steeply rising radio flares. [Matsumoto & Piran \(2023\)](#) suggest that a steep rise in the radio light curve can be obtained if a jet is observed off-axis that became visible at late times ([Sfaradi et al. 2024](#)), but it cannot account for the big jump in flux density from non-detection to detection ([Horesh et al. 2021](#)). [Teboul & Metzger \(2023\)](#) propose a scenario invoking the break out of a misaligned precessing jet that is initially choked by the disk wind (also see, [Lu et al. 2024](#)), indicating a radio-emitting process that occurs at late times. It is also possible that there are multiple outflows launched at different times relative to the discovery of TDE, which might be responsible for the fast radio brightening at a later time ([Sfaradi et al. 2025](#)). While the collision between unbound stellar debris and dense gas from the inner edge of a dusty torus (which is observed to exist in Active Galactic Nuclei, AGN) can explain the fast rising radio light curve ([Lei et al. 2024](#)), the predicted radio luminosity appears too low to reconcile with the data observed in the TDE ASASSN-15oi and AT2018hyz. In addition, by simulating the TDE evolution in the presence of an AGN disk, [Chan et al. \(2019\)](#) suggests that part of outgoing debris stream will shock with surrounding gas, generating a bright and possibly delayed radio synchrotron emission, though they did not perform detailed calculations of the radio light curve.

Alternatively, if the CNM is clumpy and filled with dense clouds, the expanding TDE outflow will sweep across them, producing bright radio emission in the bow shock ([Mou & Wang 2021; Mou et al. 2022; Bu et al. 2023](#)), which can naturally explain the delayed, fast rising light curve due to the sharp edge of cloud, as well as radio rebrightenings observed in some TDEs ([Zhuang et al. 2025](#)). While many TDEs are identified in normal galaxies (e.g., [Hammerstein et al. 2023](#)), there is a growing number of TDEs that have been discovered in galaxies with pre-existing AGN activity (e.g., [Blanchard et al. 2017; Shu et al. 2018; Zhang et al. 2022; Sun et al. 2024, 2025; Veres et al. 2024](#)). For the latter case, the existence of broad-line region clouds at a sub-pc scale (e.g., [Armijos-Abendaño et al. 2022](#)) provides the necessary condition for the interaction between TDE outflow and clouds, allowing for investigating in detail on the physical process and the resulting radio emission properties.

AT2018cqh is a rare faint TDE that occurred in a dwarf galaxy at $z = 0.048$ ([Bykov et al. 2024](#)) and exhibited optical, X-ray and radio flares, which were likely driven by an intermediate-mass black hole. A striking feature is its delayed radio emission, characterized by a two-phase fast rising light curve ([Zhang et al. 2024](#)), the nature of which is

enigmatic. In this Letter, we report the results of the high-resolution Very Long Baseline Array (VLBA) and enhanced-Multi-Element Remotely Linked Interferometer Network (e-MERLIN) follow-up observations, as well as the analysis of the newly released data from Australian Square Kilometre Array Pathfinder (ASKAP) observations at low frequency, extending to $\delta t \sim 2510$ days since optical discovery (MJD = 58285, [Zhang et al. 2024](#)). We find a peculiar radio spectral evolution peaking toward a higher frequency and flux density over a period of ~ 1000 days. Moreover, while the light curves continue to rise, there is a bump feature lasting for 240 days, with a fast rise to peak time of only 115 days. These properties are distinct from other TDEs, and point to the scenario that an outflow is launched around the time of optical discovery and interacting with dense clouds at a sub-pc scale. This is possible as the host of AT2018cqh can be spectroscopically classified as a type 2 AGN and the dense clouds are likely coming from a pre-existing broad-line region. The observations and data reductions are described in Section 2. In Section 3, we present the detailed analysis of radio morphology, flux and SED evolution properties. In Section 4, we perform hydrodynamic simulations to explore the origin of the peculiar radio flux and SED evolution in the context of the interaction between outflow and surrounding clouds. We summarize the results in Section 5. Throughout this paper, we assume a cosmology with $H_0 = 70 \text{ km s}^{-1} \text{ Mpc}^{-1}$, $\Omega_M = 0.3$, and $\Omega_\Lambda = 0.7$, corresponding to a scale of $0.941 \text{ pc milliarcsec}^{-1}$ at the redshift of AT2018cqh.

2. OBSERVATIONS AND DATA REDUCTION

2.1. *e-MERLIN*

To investigate possible radio flux and SED evolution of AT2018cqh, we performed follow-up radio observations using e-MERLIN. e-MERLIN is a UK-based radio interferometer with a maximum baseline of 217 km and seven dishes spanning 25–76 m in diameter. The facility can observe at L -, C -, and K -band. The e-MERLIN observations of AT2018cqh were completed on 2024 Sep 28 at L band (central frequency of 1.51 GHz) and on 2024 Sep 02 at C band (central frequency of 5.07 GHz) (project code: CY18012). The bandwidth is 0.52 GHz for L -band and 0.51 GHz for C -band, respectively. Data calibration was performed with the e-MERLIN Common Astronomy Software Applications (CASA) pipeline ([Moldon 2021](#)) using standard techniques. Bright radio emission components are detected in both bands. We used the `IMFIT` task in CASA to fit the radio emission with a two-dimensional elliptical Gaussian model to determine the position, integrated flux density, and peak flux density. The radio emission at both bands is unresolved and no extended emission is detected. e-MERLIN detects a compact source in the final cleaned image, which has a clean beam size of $0.41'' \times 0.13''$ at 1.51 GHz, $0.12'' \times 0.04''$ at

Table 1. Summary of the radio observations of AT2018cqh

| Observatory | Project | ν | Date | Phase | F_ν | rms |
|-------------|---------|-------|-------------|--------|--------------------|------------|
| | | (GHz) | | (days) | (mJy/beam) | (mJy/beam) |
| ASKAP | RACS | 1.66 | 2022 Jan 08 | 1302 | 3.331 ± 0.080 | 0.183 |
| ASKAP | VAST | 0.89 | 2023 Dec 26 | 2019 | 6.640 ± 0.160 | 0.252 |
| | RACS | 0.94 | 2024 Jan 03 | 2027 | 8.880 ± 0.130 | 0.165 |
| | VAST | 0.89 | 2024 Mar 02 | 2086 | 4.240 ± 0.210 | 0.249 |
| | VAST | 0.89 | 2024 Apr 27 | 2142 | 4.770 ± 0.150 | 0.298 |
| | VAST | 0.89 | 2024 Jun 21 | 2197 | 6.250 ± 0.160 | 0.306 |
| | VAST | 0.89 | 2024 Aug 21 | 2258 | 6.960 ± 0.160 | 0.230 |
| | VAST | 0.89 | 2024 Oct 22 | 2320 | 6.260 ± 0.150 | 0.226 |
| | VAST | 0.89 | 2024 Dec 21 | 2380 | 9.330 ± 0.170 | 0.231 |
| | VAST | 0.89 | 2025 Feb 22 | 2443 | 6.510 ± 0.140 | 0.235 |
| | VAST | 0.89 | 2025 Apr 21 | 2510 | 11.80 ± 0.250 | 0.267 |
| VLBA | BS340B | 1.56 | 2024 Aug 04 | 2241 | 10.91 ± 0.780 | 0.356 |
| | BS340A | 4.74 | 2024 Aug 06 | 2243 | 16.023 ± 0.056 | 0.076 |
| | | 7.63 | 2024 Aug 06 | 2243 | 11.574 ± 0.044 | 0.061 |
| e-MERLIN | CY18012 | 1.51 | 2024 Sep 28 | 2297 | 10.310 ± 0.380 | 0.220 |
| | | 5.07 | 2024 Sep 02 | 2270 | 12.210 ± 0.180 | 0.147 |
| uGMRT | ddtC411 | 1.26 | 2024 Dec 29 | 2388 | 14.120 ± 0.380 | 0.075 |
| | | 0.75 | 2025 Jan 25 | 2415 | 5.250 ± 0.280 | 0.274 |
| | | 1.26 | 2025 Jan 26 | 2416 | 20.620 ± 0.650 | 0.056 |
| | | 0.75 | 2025 Feb 21 | 2442 | 5.680 ± 0.350 | 0.496 |
| | | 1.26 | 2025 Feb 20 | 2441 | 23.120 ± 0.270 | 0.066 |
| | | 0.75 | 2025 Mar 24 | 2473 | 4.600 ± 0.530 | 0.466 |
| | | 1.26 | 2025 Mar 22 | 2471 | 19.600 ± 0.260 | 0.070 |

5.07 GHz. We obtained a peak flux density of 10.31 ± 0.38 mJy/beam at L band and 12.21 ± 0.18 mJy/beam at C band, respectively. Note the the integrated and peak flux densities are roughly equal to each other at both bands, as expected for a compact radio source. Therefore, for consistency, only peak flux densities are used in our following analysis. The e-MERLIN observational log and flux density measurements are presented in Table 1.

2.2. VLBA

The VLBA observations of AT2018cqh were carried out on 2024 Aug 04 at L band (central frequency of 1.57GHz) and on 2024 Aug 06 at C band (central frequencies of 4.74GHz and 7.63GHz) (project code: BS340). Seven antennas were participated in the observations (BR, FD, HN, NL, OV, PT, and SC for L band observation; BR, FD, HN, MK, NL, PT, and SC for C band observation). The observations were performed in the phase-referencing mode. The bright source J0239-0234 (\sim 420 mJy at 5GHz, about 2.15° from the target) was used as the phase-reference calibrator. Phase-reference cycle times were 4.5 minutes, with 3.5 minutes on-

source and 1.0 minutes for the phase calibrator. We also inserted several scans of the bright source 3C84 for fringe and bandpass calibration with an integration time for each scan of 4 minutes at L band and 3 minutes at C band, respectively. To check the calibration results, we also inserted several scans of a bright source J0223-0205 (\sim 120 mJy at 8.7GHz, about 2.85° from the target) with an integration time of 2 minutes for each scan. The resulting total on-source time was 2 hours for L band and 4 hours for C band, respectively. To achieve sufficiently high imaging sensitivity, we adopted the observational mode Digital Down-converter System for Roach Digital Backend to use the largest recording rate of 2 Gbps, corresponding to a recording bandwidth of 128 MHz in each of the dual circular polarizations. The data from the VLBA experiment were correlated with the DiFX software correlator (Deller et al. 2011). We used the NRAO AIPS software to calibrate the amplitudes and phases of the visibility data, following the standard procedure from the AIPS Cookbook¹.

¹ <http://www.aips.nrao.edu/cook.html>

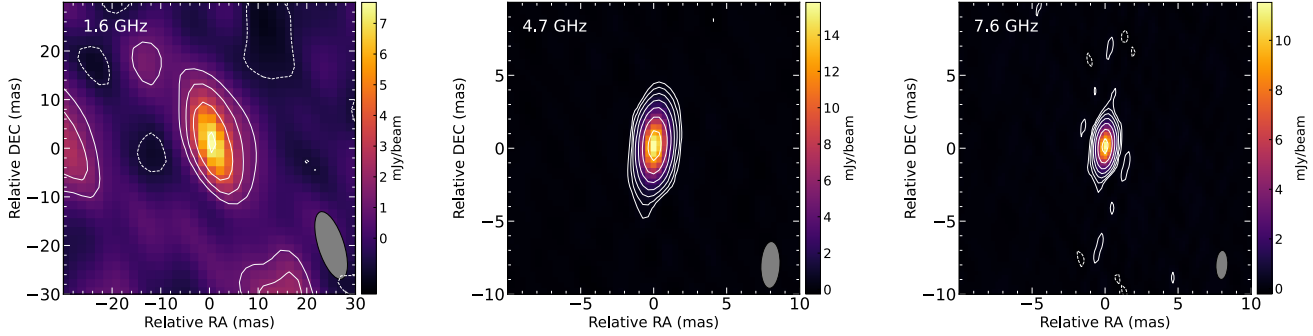


Figure 1. Natural-weighted images of VLBA observations of AT 2018cqh at three frequencies. In each image, the bottom right ellipse is the shape of the restoring beam, with sizes of 14.51×5.29 mas for L-band, 3.20×1.30 mas for C-band, and 1.99×0.81 mas for X-band, respectively. The contour levels are $2.5\sigma \times (-1, 1, 2, 4, 8)$ for L-band, and $2.5\sigma \times (-1, 1, 2, 4, 8, 16, 32, \text{and } 64)$ for C-band and X-band.

The calibrated data were imported into the Caltech DIFMAP package (Shepherd 1997) for imaging and model fitting. We then measured the flux densities at 1.6 GHz, 4.7 GHz and 7.6 GHz, following the procedures described in Section 2.1. The results are given in Table 1².

2.3. *uGMRT*

AT2018cqh was observed with the upgraded Giant Metrewave Radio Telescope (*uGMRT*) at band4 (central frequencies of 0.75 GHz) on 2025 Jan 03, 2025 Jan 25, 2025 Feb 21, and 2025 Mar 24, and at band5 (central frequencies of 1.26 GHz) on 2024 Dec 29, 2025 Jan 26, 2025 Feb 20, and 2025 Mar 22 (project code: ddtC411). Flux calibration was conducted using 3C 48, whereas the nearby source 0217+017 was also used to determine the complex gain solutions. The band4 observation performed on 2024 Jan 03 could not be imaged due to the absence of radio interferometric fringes from the phase calibrator. The data from the *uGMRT* observations were reduced using CASA (version 5.6.1) following standard procedures and by using a pipeline adapted from the CAAsa Pipeline-cum-Toolkit for Upgraded Giant Metrewave Radio Telescope data REduction (CAPTURE; Kale & Ishwara-Chandra 2021). We began our reduction by flagging known bad channels, and the remaining RFI was flagged with the flagdata task using the clip and tfcrop modes. We then ran the task tclean with the options of the MS-MFS (multi-scale multi-frequency synthesis, Rau & Cornwell 2011) deconvolver, two Taylor terms (nterms=2), and W-Projection (Cornwell et al. 2008) to accurately model the wide bandwidth and the non-coplanar field of view of *uGMRT*. AT2018cqh was detected in all *uGMRT* observa-

² Due to the presence of severe radio frequency interference (RFI) in the VLBA observation at *L*-band, a considerable portion of the data was flagged during calibration process. This may introduce errors in phase calibration, resulting in a relatively high image rms of ~ 0.4 mJy/beam and larger uncertainty in the peak flux. Therefore, we report the integrated flux density for the VLBA *L*-band observation that is more reliable.

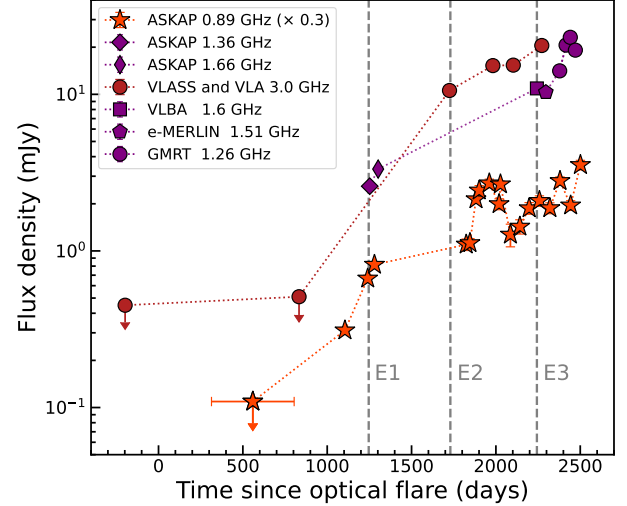


Figure 2. The radio light curves of AT 2018cqh, including the data from the ASKAP observations at 0.89 GHz, 1.36 GHz and 1.66 GHz, the e-MERLIN observations at 1.51 GHz, the VLASS observations at 3 GHz, the VLBA observations at 1.56 GHz, and the VLA observations at 3.0 GHz (Section 3.2). The radio emission appears later relative to the time of optical discovery (MJD = 58285) and shows a continuous rising in flux that can vary on time-scales down to ~ 2 months. For the nondetections, the corresponding 3σ upper limits on flux density are shown. The vertical dashed lines represent the three epochs for which the radio SED can be constrained (Figure 3), corresponding to 1246, 1730, and 2243 days after the optical discovery, respectively.

tions as an unresolved source, and the flux density measurements are shown in Table 1.

In addition, AT2018cqh was repeatedly observed at low frequencies by ASKAP Variables and Slow Transients Survey (VAST; Murphy et al. 2021), and the Rapid ASKAP Continuum Survey (RACS; McConnell et al. 2020). Here we present an uniform analysis of all archival radio data obtained with VAST and RACS, specifically, for those that are not given in Zhang et al. (2024), covering a new period from

Dec 26, 2023 to Apr 21, 2025. Table 1 presents the ASKAP observational log and flux density measurements.

3. ANALYSIS AND RESULTS

3.1. Parsec-scale Radio Morphology

In Figure 1, we show the VLBA images of AT2018cqh at 1.56, 4.74, and 7.63GHz, respectively. Because the signal-to-noise ratio of the its radio emission is high, we performed one loop phase self-calibration at C - and X -band. After several tens of fitting iterations in CASA by using an elliptical Gaussian brightness distribution model, we measured the integrated flux densities of C- and X-band which are 17.95 ± 0.12 mJy and 12.80 ± 0.091 mJy, respectively, while the corresponding peak flux densities are 16.02 ± 0.056 mJy and 11.57 ± 0.044 mJy. The ratio of the integrated and peak flux densities is 1.12 and 1.10 for C- and X-band, indicating that the radio source might be unresolved in the final imaging. The size of restoring beam³ is 14.51×5.29 mas at 1.56 GHz, 3.20×1.30 mas at 4.74 GHz, and 1.99×0.81 mas at 7.63 GHz, respectively. The deconvolved beam size is 7.66 mas \times 4.64 mas at 1.56 GHz, 0.996 mas \times 0.381 mas at 4.74 GHz, and 0.676 mas \times 0.134 mas at 7.63 GHz, respectively. To further investigate whether the source is resolved or not, we used the task `ModelFit` in DIFMAP to fit the radio emission component, but found no additional emission components in the residual map ($>3\sigma$). Therefore, AT2018cqh remains compact and unresolved at the resolution of VLBA observations, with an upper limit on its size of < 0.126 pc by using the deconvolved beam size of 7.63 GHz.

The brightness temperature of compact radio emission can be estimated as (e.g., Ulvestad et al. 2005)

$$T_b = 1.8 \times 10^9 (1+z) \left(\frac{S_\nu}{1 \text{ mJy}} \right) \left(\frac{\nu}{1 \text{ GHz}} \right)^{-2} \left(\frac{\theta_1 \theta_2}{1 \text{ mas}^2} \right)^{-1} \quad (1)$$

where S_ν is the peak flux density in mJy at the observing frequency ν in GHz, with θ_1 and θ_2 being the fitted Full Width at Half Maximum (FWHM) of the major and minor axes of the Gaussian component in units of milliarcseconds. Using the peak flux density and upper limit on the deconvolved source size derived from the VLBA 7.6 GHz image, we obtained a brightness temperature of $T_b \gtrsim 4.03 \times 10^9$ K. This T_b limit significantly exceeds the brightness temperature threshold of normal star-formation process (typically $\leq 10^5$ K, Condon 1992), suggesting that the VLBA component in AT2018cqh is clearly of non-thermal origin. The brightness temperature is lower than the equipartition temperature of 5×10^{10} K (Readhead 1994), and also much less

than the limiting brightness temperature of $\sim 10^{12}$ K due to the inverse Compton catastrophe (Kellermann et al. 1969). This implies that the compact radio emission could not be associated with a jet, or the jet could have a low Doppler factor. Such a scenario could be further investigated with future VLBI observations to measure potential proper motion of the radio emission.

3.2. Radio Light Curves: Continued Brightening

Figure 2 presents the radio light curves of AT2018cqh, at 0.89 GHz observed by ASKAP, 1.3-1.6 GHz observed by ASKAP, GMRT, e-MERLIN and VLBA, and 3 GHz observed by Very Long array (VLA). Note that in addition to data provided in Table 1 and Zhang et al. (2024), we retrieved the 3 GHz data observed by VLA (project code: 23B-321; PI: Collin Christy), consisting of three-epoch observations between Nov 19, 2023 and Sep 4, 2024. We then produced the calibrated clean images, and measured the flux densities at 3 GHz, following the procedures described in Yang et al. (2022). As shown in Figure 2, the 3 GHz flux displays a continuous rising trend. Zhang et al. (2024) fitted the temporal evolution of the VLA Long Array Sky Survey (VLASS) 3 GHz flux with a power-law index $\alpha > 4.2$, which becomes shallower ($\alpha = 2.23$) if taking into account the data from the VLA follow-up observations at the same band. The light curve at 0.89 GHz observed by ASKAP exhibits a bump feature at $\delta t \approx 1846 - 2086$ days relative to the time of the optical discovery. Following the bump in the light curve, the 0.89 GHz emission starts to rise again towards higher flux levels, but with fluctuations down to ~ 2 months. To quantify the amplitude of the flux fluctuation, we perform a linear fit to the flux evolution starting at $\delta t = 2086$ days, and then subtract this baseline to obtain variability amplitudes in the range of 7.4% - 27.5%, with a median of 10.8%.

It is well known that the effect of interstellar scintillation (ISS) could cause intraday radio variability in some AGNs with compact radio emission (Lovell et al. 2003; Rickett 2007), especially at lower frequencies. We investigate whether the observed radio variability in AT2018cqh might be induced by the ISS effect, given the small source size of ~ 134 micro-arcsecond (μ as) at 7.6 GHz measured by VLBA (Section 3.1). Using the NE2001 electron density model (Cordes & Lazio 2002), we infer that for the Galactic coordinates of AT2018cqh the transition frequency between strong and weak scintillation regimes occurs at ~ 6.69 GHz and the angular size limit of the first Fresnel zone at the transition is 5.8μ as. Adopting the formalisms provided in Walker (1998) and the angular size of $\sim 134 \mu$ as obtained by VLBA, we estimate that the level of frequency-dependent random flux variations induced by the refractive ISS is from 32% at 0.89 GHz to 13% at 3 GHz for AT2018cqh, with the time-scale for the modulation of 169 h (7 d) and 34 h (1.4 d),

³ The restoring beam is an idealized elliptical Gaussian that approximates the main lobe of the dirty beam. It is determined by the UV coverage of the array.

respectively. Given the comparable variability amplitudes, the flux fluctuations in the phase of continued radio brightening could be due to the ISS effect, though the cadence of ASKAP observations is insufficient to resolve the flux variability on shorter timescales. The ISS effect, however, cannot be the primary factor causing the bump feature in the 0.89 GHz light curve, as its variability amplitude is $>100\%$ and appears more regular.

3.3. Radio SED Evolution and Modeling

Figure 3 displays the radio SEDs of AT2018cqh. In addition to the data presented in Zhang et al. (2024), we have incorporated new measurements on the SEDs from quasi-simultaneous VLBA and e-MERLIN observations. Interestingly, although with higher spatial resolution, it is clear that the SED has evolved to peak at higher frequency and flux density. To quantify the SED evolution, we fit the SED with a synchrotron emission model in the standard framework of a non-relativistic outflow expanding into and shocking the CNM with a density profile $n \propto r^{-k}$. We use the synchrotron spectrum 2 described by Granot & Sari (2002), assuming $\nu_m \ll \nu_a$, where ν_m is the characteristic synchrotron frequency of the emitting electrons with the least energy and ν_a is the self-absorption frequency. Such a model has been widely used to explain the radio emission from non-relativistic TDEs (e.g., Alexander et al. 2016; Goodwin et al. 2022).

We then employ an Markov Chain Monte Carlo (MCMC) fitting technique (python module `emcee`; Foreman-Mackey et al. 2013) to marginalize over the synchrotron model parameters to determine the best-fitting parameters and uncertainties. Owing to the sparse sampling of the radio SED, especially at higher frequencies, we fix the synchrotron energy index in the optically thin regime to $p = 3$ (e.g., Alexander et al. 2016; Cendes et al. 2021). In Figure 3, we show the resulting SED models, which provide reasonable fits to the data. From the best-fitting SED models, we determine the peak flux density and frequency, $F_{\nu,p}$ and ν_p , respectively. We find that both $F_{\nu,p}$ and ν_p increase steadily with time, from 2.47 mJy and 1.42 GHz to 18.73 mJy and 3.22 GHz over a period of 997 days. Using the inferred values of $F_{\nu,p}$ and ν_p , we can further adopt an equipartition analysis to derive the radius of the radio-emitting region (R_{eq}) and kinetic energy (E_{eq}) using the scaling relations outlined in Barniol Duran et al. (2013). Following the procedures described in Goodwin et al. (2022), we provide constraints for two different geometries, a spherical outflow and a mildly collimated conical outflow with a half-opening angle of $\phi = 30^\circ$, in order to account for the possible geometric dependence of outflow evolution.

Through the equipartition analysis, we derive the temporal evolution of physical parameters in the radio-emitting region

over three epochs. As shown in Figure 4, for the spherical outflow, we find that the radius remains nearly constant, ranging from $R_{eq} \approx 2.04 \times 10^{17}$ cm to $\approx 2.52 \times 10^{17}$ cm between $\delta t = 1246$ and 2243 days, while the ambient density increases by a factor of ~ 3 , with n_e increasing from ≈ 1017.6 cm $^{-3}$ to ≈ 3409.1 cm $^{-3}$ over the same period. Note that assuming a mildly collimated outflow yields a similar evolution in the parameters of R_{eq} and n_e . Such an evolution in the equipartition radius and the ambient density is inconsistent with the continued radio brightening at low frequencies (Section 3.2), thus seems to disfavor the predictions of the standard CNM shockwave model.

We note that the flux in ~ 5 GHz observed by e-MERLIN on Sep 2, 2024 is a factor of ~ 1.5 lower than the 4.7 GHz flux observed by VLBA on Aug 6, 2024, while the flux in ~ 1.5 GHz is consistent with each other. Such a flux difference cannot be due to the errors in flux measurements, as the target is bright. The ISS-induced variability ($\sim 5\%$) seems unlikely to explain the 5 GHz flux decrease observed by e-MERLIN. Considering that the spatial resolution of the e-MERLIN observations is a factor of ≈ 30 larger than VLBA at the same band, the flux variability seems intrinsic to source and not due to the resolution effect. This suggests that there is a potentially slow evolution in the radio SED peaking towards lower frequencies on a time-scale of ~ 1 month. On the other hand, the flux in the 0.89 GHz observed on Aug 21, 2024 exceeds that extrapolated from the best-fit SED model, by a factor of 2. Such an excess emission cannot be simply explained by the ISS effect, but represents intrinsic flux increase at the lower frequencies (see Figure 2). More interestingly, the recent high-cadence GMRT observations at ~ 0.7 and 1.3 GHz reveal a possibly new phase of fast flux rising. Further radio observations covering a broader frequency range are required to uncover whether there is a new pattern in the SED evolution, which is beyond the scope of current paper.

4. DISCUSSIONS

In Zhang et al. (2024), we reported the detection of delayed radio emission from the TDE AT2018cqh, which might be related to the delayed launching of outflow. However, follow-up radio observing campaigns (including our e-MERLIN and VLBA observations) reveal an unusually evolving radio emission (up to $\delta t \sim 2510$ days since its discovery). As mentioned in Section 3.2, the low-frequency radio emission displays continuous rising in flux with time. Particularly, there is a bump feature observed in the 0.89 GHz light curve between $\delta t = 1846 - 2086$ days, which cannot be explained under the standard model of an outflow interacting and shocking a homogeneous CNM. The rise to peak time of ~ 115 days for the bump seems to disfavor a more complex model involving an inhomogeneous CNM, in which the time-scale is typically \sim days (Matsumoto & Piran 2024). The radio

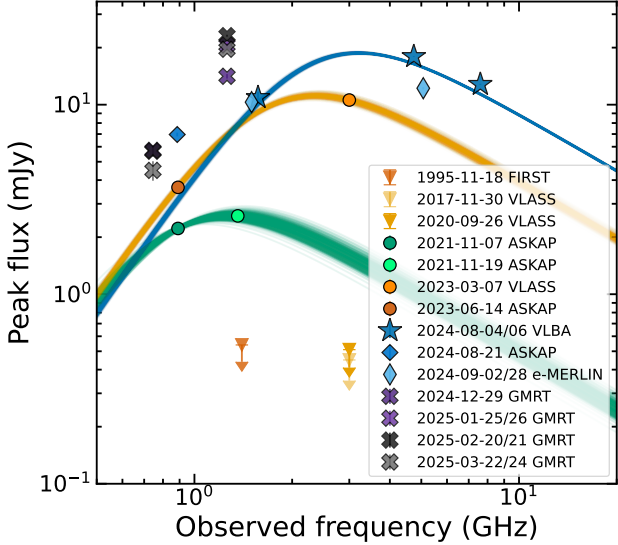


Figure 3. The radio SEDs for three epochs that have quasi-simultaneous observations at different frequencies. For the non-detections, the corresponding 3σ upper limits on flux density are shown. The green, orange and blue lines represent the best fit to each SED from our MCMC modeling (Section 3.3), which are the model realizations on a basis of 500 random samples from the MCMC chains. There is a steady rise in both peak flux density and frequency between the three epochs.

spectral evolution is also peculiar, characterized by a shift toward higher peak frequency and peak flux density. This is in contrast to the radio evolution observed in other TDEs and in hydrodynamic simulations of the interaction between TDE outflow and a spherically symmetric CNM, where the peak frequency and flux density typically decrease over time (Fangyi et al. 2025). While the increase in the peak flux density has been found in a few TDEs, the radio peak frequency does not vary or even decrease with time (Cendes et al. 2022, 2025; Christy et al. 2024), which is inconsistent with what we observed in AT2018cqh.

On the other hand, based on the analysis using the equipartition theory (Section 3.3), we found that the equipartition radius increased very little over a period of $\sim 1,000$ days between $\delta t = 1246$ and 2243 days. This suggests that if the equipartition radius corresponds to the forward shock radius driven by the outflow in the CNM, its velocity during this period would be only about $0.018c$ for the spherical outflow case. By contrast, the shock velocity during the first 1246 days can be as high as $0.063c$. If we take into account the possibility of a delayed outflow, the shock velocity would be even higher. Based on the inferred CNM densities (1017.6 and 3409.1 cm $^{-3}$, Figure 4), we estimate that the kinetic energy of post shock CNM in the period of 1246–2243 days is about half of that in the first 1246 days. According to the Rankine-Hugoniot conditions, the internal energy of post-shock CNM is comparable to its kinetic energy. This

indicates that about half of the energy is dissipated within the 1000 days. However, radiative cooling cannot dissipate this energy, as the cooling timescale (exceeding 1000 years, Sutherland & Dopita 1993) far exceeds the observed period. This challenges the self-consistency of the standard outflow–CNM model widely used in literature.

4.1. Outflow–cloud interaction

As mentioned above, a notable feature of the radio evolution from AT2018cqh is the presence of fluctuations in the flux, particularly the bump feature. The bump feature indicates a significant drop in flux by a factor of 2 over a timescale of 2 months ($\delta t = 2027 - 2086$ days), with the magnitude exceeding that caused by interstellar scintillation. This provides crucial clues for uncovering the physical origin of the radio flares. If it is generated by the outflow–CNM scenario, for affecting the overall radiation zone sized of 2×10^{17} cm (Figure 4), perturbations should go with a velocity higher than the light speed, suggesting that the conventional outflow–CNM scenario may lead to an inconsistent result. The aforementioned discrepancies could be naturally resolved by introducing the outflow–cloud interaction model: (1) outflow impacting multiple clouds (Mou & Wang 2021; Mou et al. 2022; Zhuang et al. 2025); or (2) non-smooth outflow (with varying density) impacting one single cloud. The dense clouds are likely present in the circumnuclear environment of AT2018cqh, as its host can be classified as a type 2 AGN (Zhang et al. 2024). Thus, we examine the scenario of the outflow–cloud interaction by using hydrodynamic simulations. Due to the poor knowledge of the TDE outflow and the circumnuclear environment, we make simplifications to the physical parameters in simulations, while the model parameters that successfully fit the observations are not unique.

4.1.1. Model Settings

We conducted simulations with the ZEUS-3D code (Clarke 2010), which includes the cosmic ray electrons (CRe) as a second fluid. For simplicity, we did not incorporate the magnetic field and diffusion of CRe. The hydrodynamic equations are

$$\frac{\partial \rho}{\partial t} + \nabla \cdot (\rho \mathbf{v}) = 0, \quad (2)$$

$$\rho \frac{d\mathbf{v}}{dt} = -\nabla(p_1 + p_2) - \rho \nabla \Phi, \quad (3)$$

$$\frac{\partial e_1}{\partial t} + \nabla \cdot (e_1 \mathbf{v}) = -p_1 \nabla \cdot \mathbf{v}, \quad (4)$$

$$\frac{\partial e_2}{\partial t} + \nabla \cdot (e_2 \mathbf{v}) = -p_2 \nabla \cdot \mathbf{v}, \quad (5)$$

where $p_1 \equiv (\gamma_1 - 1)e_1$ is the thermal pressure ($\gamma_1 = 5/3$), $p_2 \equiv (\gamma_2 - 1)e_2$ is the pressure of CRe ($\gamma_2 = 4/3$), and Φ is the gravitation potential ($\Phi = -GM_{\text{bh}}/r$). We did not

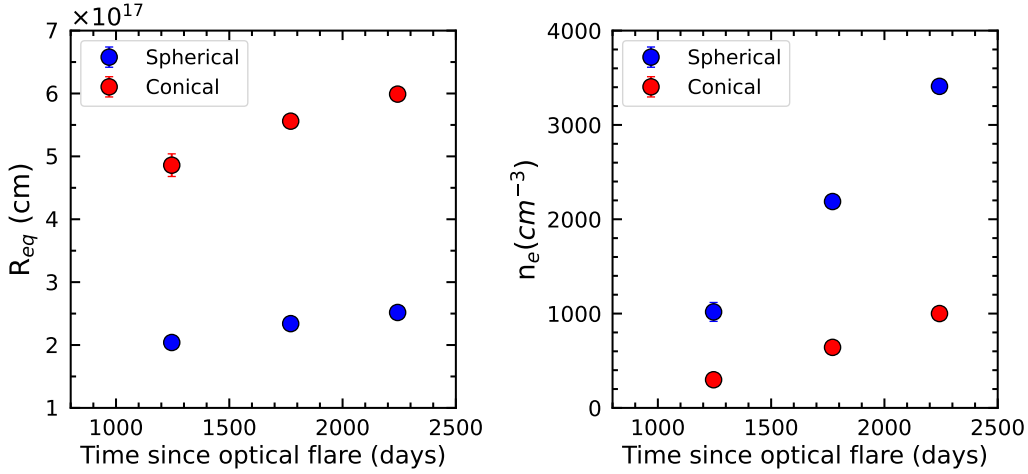


Figure 4. The evolution of radius (left) and kinetic energy (right) as a function of time from our equipartition analysis, assuming a single outflow is launched into the CNM around the time of optical discovery. Blue and red filled circles indicate parameters for a spherical homogeneous and a collimated conical outflow, respectively.

simulate the acceleration process of electrons, but instead, directly injected the CRe component as the second fluid which is embodied as the energy density e_2 . As mentioned in the next subsection, e_2 is assigned the value of $\frac{5}{3} \epsilon_e e_d$, where e_d is thermal pressure in the downstream. The shock front in ZEUS-3D is typically captured with 4 meshes, and thus we inject the CRe at the 4th-mesh when the parameters of the post-shock gas have been stabilized. The simulation domain is 2.5 dimensional spherical coordinates, of which the system is symmetric in ϕ -direction. The initial density distribution of the hot CNM is assumed in a form of $\rho_{\text{cnm}}(r) = \rho_0 r^{-n}$. Here we set it to be the same as the density distribution of the Galactic Center, i.e., $\rho_{\text{cnm}}(r) = 3 \text{ m}_H \text{ cm}^{-3} (r/\text{pc})^{-1}$ (Gillessen et al. 2019).

Using the radio SED from three epochs, and applying the minimal energy method (Barniol Duran et al. 2013), we find that the sizes of the radiation zones of three epochs ($\delta t = 1246$, 1730, and 2243 days in the observer's frame) show tiny difference despite a time span of 1000 days. Thus, it is possible that the outflow continuously interacts with one single cloud. By performing a serial of simulations, we find that such a scenario successfully reproduces the radio flares of AT2018cqh. Specifically, the cloud is assumed to be spherical shape with a radius of 0.08 pc, and its center is placed at the polar axis with a distance of 0.43 pc from the SMBH. The TDE outflow is injected at the inner boundary of the simulation domain for $t \leq 1.6$ years, and is confined within two cones along the bipolar directions, whose total solid angle is $0.1 \times 4\pi \text{ sr}$ (corresponding to a half-opening angle of 25.8°). The outflow velocity decreases linearly from 0.5 c to 0.2 c, and the mass outflow rate increases with time:

$$\dot{M}_{\text{out}}(t) = 0.006 M_{\odot} \text{ yr}^{-1} \cdot \left[2 + 100 \times \left(\frac{t}{1.6 \text{ yr}} \right)^3 \right]. \quad (6)$$

4.1.2. Relativistic Electrons and Magnetic Field

The electron acceleration efficiency ϵ_e is assumed to be the fraction of the energy flux that can be dissipated at the shock surface (i.e., the change in the kinetic energy flux across the shock) channelled into the accelerated relativistic electrons in the downstream. In the frame of shock front, the acceleration efficiency is

$$\epsilon_e = \frac{e_2 v_d}{\frac{1}{2} \rho_i v_s^3 (1 - C^{-2})} \quad (7)$$

where e_2 is the energy density of CRe in the downstream, v_d is the downstream velocity, ρ_i is the pre-shock density, and $C = 4M^2/(M^2 + 3)$ is the compression ratio. When the Mach number $M \gg 1$, we have $v_d = v_s/4$ and $C = 4$. In this case, the above equation can be further simplified as $\epsilon_e = 0.6e_2/e_d$, where e_d is thermal pressure in the downstream.

We did not include the magnetic field in the simulations, and simply assumed that the energy ratio of magnetic field to CRe in each mesh remains constant, i.e., $[B^2/(8\pi)]/e_2 = \epsilon_b/\epsilon_e = \text{constant}$. We set $\epsilon_b = \epsilon_e = 0.1$ in this study. We present the density distribution and CRe's energy density distribution for different moments.

4.1.3. Simulation Results

Our simulations can provide the distribution of CR and the magnetic field strength at any given moment, thereby yielding the radio spectrum at that moment. However, the radiation zone formed by the bow shock is not spherically symmetric, and the radio SED varies with line of sight. Here we simplify the situation by treating the radiation zone as a radiation shell surrounding the spherical cloud, where the CRe's energy density and magnetic field strength inside are uniform. According to hydrodynamic simulations (see Figure. 5), the radiation shell is thin compared to the cloud, with an approximate thickness of ~ 0.01 pc. We assume,

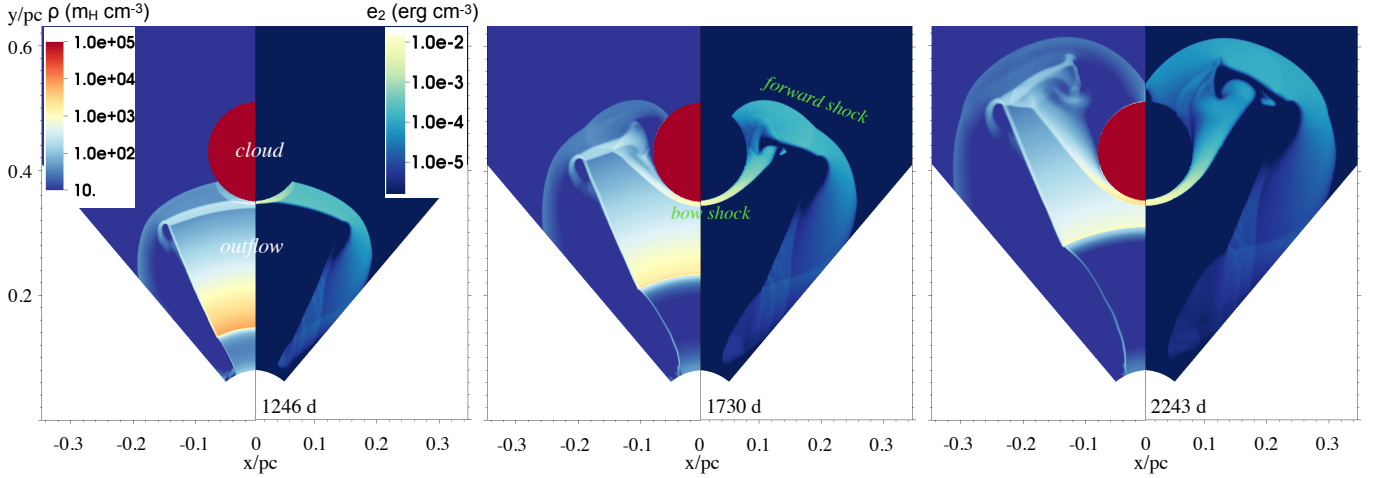


Figure 5. Evolution for the outflow–cloud interaction. Panels from the *left* to the *right* show the density and CRe energy at three different epochs (observer’s frame): $\delta t = 1246$ d, 1730 d and 2243 d.

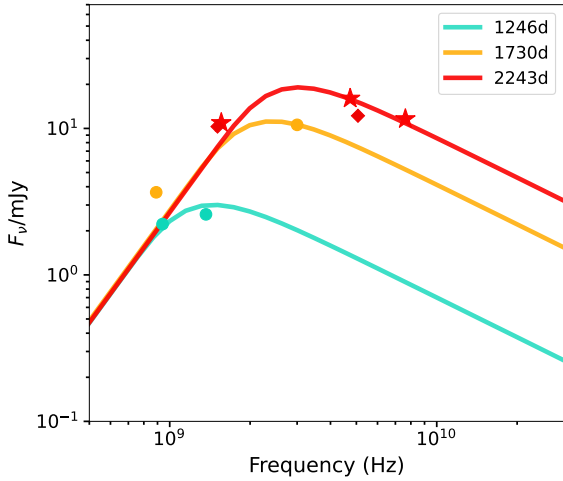


Figure 6. Hydrodynamic modeling of the radio SEDs of AT2018cqh. The cyan, orange and red lines correspond to the model SEDs at $\delta t = 1246$ d, 1730 d and 2243 d in observer’s frame, respectively. The filled circles, stars and diamonds represent the observed flux densities, as shown in Figure 3.

approximately, that the radiative zone is a thin spherical shell with a radius of 0.09 pc and a thickness of 0.01 pc. The CReS per unit volume follow a power-law distribution: $dn(E)/dE = AE^{-p}$, where the coefficient $A \propto e_2$, and we fix the index $p = 2.8$. The synchrotron emission spectrum per unit volume can be computed as:

$$j_\nu \propto AB^{\frac{p+1}{2}} \propto \left(8\pi \frac{\epsilon_b}{\epsilon_e}\right)^{\frac{p+1}{4}} e_2^{\frac{p+5}{4}} \quad (8)$$

To obtain the total synchrotron radiation from the volume integration, we use the following approximation: $\int \left(8\pi \frac{\epsilon_b}{\epsilon_e}\right)^{\frac{p+1}{4}} e_2^{\frac{p+5}{4}} dV = \bar{B}^{\frac{p+1}{2}} \int e_2 dV$, where the equiv-

alent magnetic field strength is

$$\bar{B} = \left[\left(8\pi \frac{\epsilon_b}{\epsilon_e}\right)^{\frac{p+1}{4}} \cdot \frac{\int e_2^{\frac{p+5}{4}} dV}{\int e_2 dV} \right]^{\frac{2}{p+1}} \quad (9)$$

Using such a simplified radiation shell, the total energy of CRe from simulations ($\int e_2 dV$) and the equivalent magnetic field strength \bar{B} , we calculate the self-absorbed radio spectrum. The radio SEDs from our simulations are shown in Figure 6, which can match the observed radio SEDs at three epochs for the outflow–cloud-interaction picture.

Through simulations, we demonstrate that the SED evolution of AT2018cqh can be constrained within the theoretical framework of outflow–cloud interaction. The size of the emission region – that is, the size of the bow shock – is roughly comparable to the size of the cloud, and therefore shows no significant change over the duration of 1000 days (from 1246 to 2243 days). This is also consistent with the absence of a resolved component in the VLBA imaging observations.

5. CONCLUSIONS

We present follow-up VLBA and e-MERLIN radio observations of AT2018cqh extending to $\delta t \sim 2250$ days post discovery. With the high resolution imaging at a mas-scale, VLBA reveals a compact radio emission unresolved at a physical scale of $\lesssim 0.13$ pc at 7.6 GHz, with a brightness temperature of $T_b \gtrsim 4 \times 10^9$ K. In addition to the core, e-MERLIN observation at 5 GHz does not detect any extended emission components at a scale of 34.6 pc, supporting the compactness of the radio emission. The quasi-simultaneous VLBA and e-MERLIN observations allow for constraining the radio spectral evolution at later times, and find a shift in the SED to a higher peak flux density and frequency. Such a

radio SED evolution is unprecedented among known TDEs. The radio light curve at 0.89 GHz observed with ASKAP suggests a continued flux increase, with a bump feature at $\delta t \approx 1846$ days. The radio flux and SED evolution properties of AT2018cqh are inconsistent with the predictions of conventional outflow-CNM interaction model, but can be naturally explained by the outflow-cloud interaction. We verified the latter model by hydrodynamic simulations and found that it can reproduce the peculiar radio SED evolution observed in AT2018cqh.

Since the most recent GMRT observations at ~ 0.7 and 1.3 GHz find a possibly new phase of fast flux rising, continued radio observations covering a broader frequency range are required to catch the peak of the radio SED, uncovering whether there is a new pattern in the SED evolution. With new radio observations, the outflow–cloud interaction model can be tested in detail through comparisons with hydrodynamic simulations. In addition to radio flares, theoretical studies demonstrate that the outflow–cloud interaction is capable of generating X-ray emission when the cloud shock propagates through the cloud (Mou et al. 2021). Based on our simulation data (Section 4.1.1), the intrinsic X-ray luminosity in 0.3–10 keV range is inferred to be $L_X \approx 10^{41}$ erg s $^{-1}$, which is an order of magnitude lower than those obtained from the recent XMM-Newton and Swift/XRT observations (Wang et al. 2025, private communication). The X-ray spectrum of AT2018cqh is currently dominated by a thermal blackbody component ($kT \approx 60$ eV) likely powered by the accretion process. The outflow–cloud interaction model

could be further tested with future sensitive X-ray observations, once the TDE’s thermal disk emission has decayed.

We thank the anonymous referee for the constructive suggestions and detailed comments, which helped to improve the clarity and quality of this paper. We thank the staff of the e-MERLIN, VLBA and GMRT, that made these observations possible. e-MERLIN is a National Facility operated by the University of Manchester at Jodrell Bank Observatory on behalf of STFC. The National Radio Astronomy Observatory is a facility of the National Science Foundation operated under cooperative agreement by Associated Universities, Inc. GMRT is run by the National Centre for Radio Astrophysics of the Tata Institute of Fundamental Research. The Australian SKA Pathfinder is part of the Australia Telescope National Facility, which is managed by CSIRO. Operation of ASKAP is funded by the Australian Government with support from the National Collaborative Research Infrastructure Strategy. This paper includes archived data obtained through the CSIRO ASKAP Science Data Archive, CASDA (<http://data.csiro.au>). The work is supported by the National SKA program of China (2022SKA0130102) and the National Science Foundation of China (NSFC) through grant No. 12192220, 12192221. X.S. acknowledges the science research grants from the China Manned Space Project with NO. CMS-CSST-2025-A07. G.M. was supported by the NSFC (No. 12473013, 12133007). Y.X. was supported by the NSFC (No. 12025303).

REFERENCES

Alexander, K. D., Berger, E., Guillochon, J., Zauderer, B. A., & Williams, P. K. G. 2016, ApJL, 819, L25, doi: [10.3847/2041-8205/819/2/L25](https://doi.org/10.3847/2041-8205/819/2/L25)

Alexander, K. D., van Velzen, S., Horesh, A., & Zauderer, B. A. 2020, SSRv, 216, 81, doi: [10.1007/s11214-020-00702-w](https://doi.org/10.1007/s11214-020-00702-w)

Alexander, K. D., Wieringa, M. H., Berger, E., Saxton, R. D., & Komossa, S. 2017, ApJ, 837, 153, doi: [10.3847/1538-4357/aa6192](https://doi.org/10.3847/1538-4357/aa6192)

Andreoni, I., Coughlin, M. W., Perley, D. A., et al. 2022, Nature, 612, 430, doi: [10.1038/s41586-022-05465-8](https://doi.org/10.1038/s41586-022-05465-8)

Armijos-Abendaño, J., López, E., Llerena, M., & Logan, C. H. A. 2022, MNRAS, 514, 1535, doi: [10.1093/mnras/stac1442](https://doi.org/10.1093/mnras/stac1442)

Barniol Duran, R., Nakar, E., & Piran, T. 2013, ApJ, 772, 78, doi: [10.1088/0004-637X/772/1/78](https://doi.org/10.1088/0004-637X/772/1/78)

Blanchard, P. K., Nicholl, M., Berger, E., et al. 2017, ApJ, 843, 106, doi: [10.3847/1538-4357/aa77f7](https://doi.org/10.3847/1538-4357/aa77f7)

Brown, G. C., Levan, A. J., Stanway, E. R., et al. 2015, MNRAS, 452, 4297, doi: [10.1093/mnras/stv1520](https://doi.org/10.1093/mnras/stv1520)

Bu, D.-F., Chen, L., Mou, G., Qiao, E., & Yang, X.-H. 2023, MNRAS, 521, 4180, doi: [10.1093/mnras/stad804](https://doi.org/10.1093/mnras/stad804)

Burrows, D. N., Kennea, J. A., Ghisellini, G., et al. 2011, Nature, 476, 421, doi: [10.1038/nature10374](https://doi.org/10.1038/nature10374)

Bykov, S. D., Gilfanov, M. R., & Sunyaev, R. A. 2024, MNRAS, 527, 1962, doi: [10.1093/mnras/stad3355](https://doi.org/10.1093/mnras/stad3355)

Cendes, Y., Alexander, K. D., Berger, E., et al. 2021, ApJ, 919, 127, doi: [10.3847/1538-4357/ac110a](https://doi.org/10.3847/1538-4357/ac110a)

Cendes, Y., Berger, E., Alexander, K. D., et al. 2022, ApJ, 938, 28, doi: [10.3847/1538-4357/ac88d0](https://doi.org/10.3847/1538-4357/ac88d0)

—. 2024, ApJ, 971, 185, doi: [10.3847/1538-4357/ad5541](https://doi.org/10.3847/1538-4357/ad5541)

Cendes, Y., Berger, E., Beniamini, P., et al. 2025, arXiv e-prints, arXiv:2507.08998, doi: [10.48550/arXiv.2507.08998](https://doi.org/10.48550/arXiv.2507.08998)

Chan, C.-H., Piran, T., Krolik, J. H., & Saban, D. 2019, ApJ, 881, 113, doi: [10.3847/1538-4357/ab2b40](https://doi.org/10.3847/1538-4357/ab2b40)

Christy, C. T., Alexander, K. D., Margutti, R., et al. 2024, ApJ, 974, 18, doi: [10.3847/1538-4357/ad675b](https://doi.org/10.3847/1538-4357/ad675b)

Clarke, D. A. 2010, ApJS, 187, 119, doi: [10.1088/0067-0049/187/1/119](https://doi.org/10.1088/0067-0049/187/1/119)

Condon, J. J. 1992, *ARA&A*, 30, 575, doi: [10.1146/annurev.aa.30.090192.003043](https://doi.org/10.1146/annurev.aa.30.090192.003043)

Cordes, J. M., & Lazio, T. J. W. 2002, arXiv e-prints, astro, doi: [10.48550/arXiv.astro-ph/0207156](https://doi.org/10.48550/arXiv.astro-ph/0207156)

Cornwell, T. J., Golap, K., & Bhatnagar, S. 2008, *IEEE Journal of Selected Topics in Signal Processing*, 2, 647, doi: [10.1109/JSTSP.2008.2005290](https://doi.org/10.1109/JSTSP.2008.2005290)

De Colle, F., Guillochon, J., Naiman, J., & Ramirez-Ruiz, E. 2012, *ApJ*, 760, 103, doi: [10.1088/0004-637X/760/2/103](https://doi.org/10.1088/0004-637X/760/2/103)

Deller, A. T., Brisken, W. F., Phillips, C. J., et al. 2011, *PASP*, 123, 275, doi: [10.1086/658907](https://doi.org/10.1086/658907)

Fangyi, Hu, Goodwin, A., et al. 2025, arXiv e-prints, arXiv:2507.01273, doi: [10.48550/arXiv.2507.01273](https://doi.org/10.48550/arXiv.2507.01273)

Foreman-Mackey, D., Hogg, D. W., Lang, D., & Goodman, J. 2013, *PASP*, 125, 306, doi: [10.1086/670067](https://doi.org/10.1086/670067)

Gezari, S. 2021, *ARA&A*, 59, 21, doi: [10.1146/annurev-astro-111720-030029](https://doi.org/10.1146/annurev-astro-111720-030029)

Gillessen, S., Plewa, P. M., Widmann, F., et al. 2019, *ApJ*, 871, 126, doi: [10.3847/1538-4357/aaf4f8](https://doi.org/10.3847/1538-4357/aaf4f8)

Goodwin, A. J., van Velzen, S., Miller-Jones, J. C. A., et al. 2022, *MNRAS*, 511, 5328, doi: [10.1093/mnras/stac333](https://doi.org/10.1093/mnras/stac333)

Goodwin, A. J., Miller-Jones, J. C. A., van Velzen, S., et al. 2023a, *MNRAS*, 518, 847, doi: [10.1093/mnras/stac3127](https://doi.org/10.1093/mnras/stac3127)

Goodwin, A. J., Alexander, K. D., Miller-Jones, J. C. A., et al. 2023b, *MNRAS*, 522, 5084, doi: [10.1093/mnras/stad1258](https://doi.org/10.1093/mnras/stad1258)

Goodwin, A. J., Anderson, G. E., Miller-Jones, J. C. A., et al. 2024, *MNRAS*, 528, 7123, doi: [10.1093/mnras/stae362](https://doi.org/10.1093/mnras/stae362)

Granot, J., & Sari, R. 2002, *ApJ*, 568, 820, doi: [10.1086/338966](https://doi.org/10.1086/338966)

Hammerstein, E., van Velzen, S., Gezari, S., et al. 2023, *ApJ*, 942, 9, doi: [10.3847/1538-4357/aca283](https://doi.org/10.3847/1538-4357/aca283)

Horesh, A., Cenko, S. B., & Arcavi, I. 2021, *Nature Astronomy*, 5, 491, doi: [10.1038/s41550-021-01300-8](https://doi.org/10.1038/s41550-021-01300-8)

Kale, R., & Ishwara-Chandra, C. H. 2021, *Experimental Astronomy*, 51, 95, doi: [10.1007/s10686-020-09677-6](https://doi.org/10.1007/s10686-020-09677-6)

Kellermann, K. I., Pauliny-Toth, I. I. K., & Williams, P. J. S. 1969, *ApJ*, 157, 1, doi: [10.1086/150046](https://doi.org/10.1086/150046)

Lei, W.-H., Yuan, Q., Zhang, B., & Wang, D. 2016, *ApJ*, 816, 20, doi: [10.3847/0004-637X/816/1/20](https://doi.org/10.3847/0004-637X/816/1/20)

Lei, X., Wu, Q., Li, H., et al. 2024, *ApJ*, 977, 63, doi: [10.3847/1538-4357/ad8ba5](https://doi.org/10.3847/1538-4357/ad8ba5)

Lovell, J. E. J., Jauncey, D. L., Bignall, H. E., et al. 2003, *AJ*, 126, 1699, doi: [10.1086/378053](https://doi.org/10.1086/378053)

Lu, W., & Kumar, P. 2018, *ApJ*, 865, 128, doi: [10.3847/1538-4357/aad54a](https://doi.org/10.3847/1538-4357/aad54a)

Lu, W., Matsumoto, T., & Matzner, C. D. 2024, *MNRAS*, 533, 979, doi: [10.1093/mnras/stae1770](https://doi.org/10.1093/mnras/stae1770)

Matsumoto, T., & Piran, T. 2023, *MNRAS*, 522, 4565, doi: [10.1093/mnras/stad1269](https://doi.org/10.1093/mnras/stad1269)

—. 2024, *ApJ*, 971, 49, doi: [10.3847/1538-4357/ad58ba](https://doi.org/10.3847/1538-4357/ad58ba)

Mattila, S., Pérez-Torres, M., Efstathiou, A., et al. 2018, *Science*, 361, 482, doi: [10.1126/science.ao4669](https://doi.org/10.1126/science.ao4669)

McConnell, D., Hale, C. L., Lenc, E., et al. 2020, *PASA*, 37, e048, doi: [10.1017/pasa.2020.41](https://doi.org/10.1017/pasa.2020.41)

Moldon, J. 2021, eMCP: e-MERLIN CASA pipeline, *Astrophysics Source Code Library*, record ascl:2109.006

Mou, G., Wang, T., Wang, W., & Yang, J. 2022, *MNRAS*, 510, 3650, doi: [10.1093/mnras/stab3742](https://doi.org/10.1093/mnras/stab3742)

Mou, G., & Wang, W. 2021, *MNRAS*, 507, 1684, doi: [10.1093/mnras/stab2261](https://doi.org/10.1093/mnras/stab2261)

Mou, G., Dou, L., Jiang, N., et al. 2021, *ApJ*, 908, 197, doi: [10.3847/1538-4357/abd475](https://doi.org/10.3847/1538-4357/abd475)

Murphy, T., Kaplan, D. L., Stewart, A. J., et al. 2021, *PASA*, 38, e054, doi: [10.1017/pasa.2021.44](https://doi.org/10.1017/pasa.2021.44)

Pasham, D. R., Cenko, S. B., Levan, A. J., et al. 2015, *ApJ*, 805, 68, doi: [10.1088/0004-637X/805/1/68](https://doi.org/10.1088/0004-637X/805/1/68)

Rau, U., & Cornwell, T. J. 2011, *A&A*, 532, A71, doi: [10.1051/0004-6361/201117104](https://doi.org/10.1051/0004-6361/201117104)

Readhead, A. C. S. 1994, *ApJ*, 426, 51, doi: [10.1086/174038](https://doi.org/10.1086/174038)

Rees, M. J. 1988, *Nature*, 333, 523, doi: [10.1038/333523a0](https://doi.org/10.1038/333523a0)

Rickett, B. J. 2007, *Astronomical and Astrophysical Transactions*, 26, 429, doi: [10.1080/10556790701600580](https://doi.org/10.1080/10556790701600580)

Saxton, R., Komossa, S., Auchettl, K., & Jonker, P. G. 2020, *SSRv*, 216, 85, doi: [10.1007/s11214-020-00708-4](https://doi.org/10.1007/s11214-020-00708-4)

Sfaradi, I., Beniamini, P., Horesh, A., et al. 2024, *MNRAS*, 527, 7672, doi: [10.1093/mnras/stad3717](https://doi.org/10.1093/mnras/stad3717)

Sfaradi, I., Margutti, R., Chornock, R., et al. 2025, arXiv e-prints, arXiv:2508.03807, doi: [10.48550/arXiv.2508.03807](https://doi.org/10.48550/arXiv.2508.03807)

Shepherd, M. C. 1997, in *Astronomical Society of the Pacific Conference Series*, Vol. 125, *Astronomical Data Analysis Software and Systems VI*, ed. G. Hunt & H. Payne, 77

Shu, X. W., Wang, S. S., Dou, L. M., et al. 2018, *ApJL*, 857, L16, doi: [10.3847/2041-8213/aaba17](https://doi.org/10.3847/2041-8213/aaba17)

Sun, J., Guo, H., Gu, M., et al. 2025, *ApJ*, 982, 150, doi: [10.3847/1538-4357/adb724](https://doi.org/10.3847/1538-4357/adb724)

Sun, L., Jiang, N., Dou, L., et al. 2024, *A&A*, 692, A262, doi: [10.1051/0004-6361/202452380](https://doi.org/10.1051/0004-6361/202452380)

Sutherland, R. S., & Dopita, M. A. 1993, *ApJS*, 88, 253, doi: [10.1086/191823](https://doi.org/10.1086/191823)

Teboul, O., & Metzger, B. D. 2023, *ApJL*, 957, L9, doi: [10.3847/2041-8213/ad0037](https://doi.org/10.3847/2041-8213/ad0037)

Ulvestad, J. S., Antonucci, R. R. J., & Barvainis, R. 2005, *ApJ*, 621, 123, doi: [10.1086/427426](https://doi.org/10.1086/427426)

Veres, P. M., Franckowiak, A., van Velzen, S., et al. 2024, arXiv e-prints, arXiv:2408.17419, doi: [10.48550/arXiv.2408.17419](https://doi.org/10.48550/arXiv.2408.17419)

Walker, M. A. 1998, *MNRAS*, 294, 307, doi: [10.1046/j.1365-8711.1998.01238.x](https://doi.org/10.1046/j.1365-8711.1998.01238.x)

Yang, L., Shu, X., Zhang, F., et al. 2022, *ApJ*, 935, 115, doi: [10.3847/1538-4357/ac80ba](https://doi.org/10.3847/1538-4357/ac80ba)

Zhang, F., Shu, X., Yang, L., et al. 2024, ApJL, 962, L18,
doi: [10.3847/2041-8213/ad1d61](https://doi.org/10.3847/2041-8213/ad1d61)
Zhang, W. J., Shu, X. W., Sheng, Z. F., et al. 2022, A&A, 660,
A119, doi: [10.1051/0004-6361/202142253](https://doi.org/10.1051/0004-6361/202142253)

Zhuang, J., Shen, R.-F., Mou, G., & Lu, W. 2025, ApJ, 979, 109,
doi: [10.3847/1538-4357/ad9b98](https://doi.org/10.3847/1538-4357/ad9b98)